Structural Analysis of the LeaTop Morphing Leading Edge Concept

Adnan Feim, Ankit Gupta, Anton Shambalov, Daan Koppes, Martin Henkel, Sonny Lie, Thijs van Lith, Vlad Petrescu, Wouter Doppenberg

TU Delft, Faculty of Aerospace Engineering
AE2223-I group D7

June 9, 2016

Abstract

Morphing technology in aviation applications can yield increased efficiency through reducing the produced drag and noise compared to traditional mechanisms such as flaps or slats. The Leading Edge Topology (LeaTop) demonstrator is a mechanism able to deform the shape of the leading edge, also known as morphing, in order to improve aerodynamic performance. This paper aims to determine the effectiveness of the mechanism, its ability to match the target shape, as well as the structural behaviour of the skin due to the mechanism. The LeaTop demonstrator was tested by extending the internal actuator in steps, gathering strain data at each step and taking pictures to determine the deformed shape. By analyzing the strain data from the experiments it was determined that the deformation of the skin is mostly bending driven, although there were oscillations of axial strain around the stiffeners. From the analysis of the pictures, the maximum leading edge rotation was found to be 7.07° which complies with the minimum requirement of 5°, as set by the original design of the LeaTop project.

Keywords: Morphing Leading Edge Mechanism, LeaTop, Strain Analysis

Nomenclature

ε	Strain in the original coordinate system	-
$\tilde{\varepsilon}$	Strain in the transformed coordinate system	-
θ	Angle of rotation	°

I. Introduction

From a sustainable perspective, aviation contains many fields that can be improved upon regarding efficiency. Currently, airplanes use flaps and slats during the take-off and landing phase to generate the required amount of lift. However, during these manoeuvres the discontinuities between the actual wing and high-lift devices may cause the boundary layer to become turbulent, resulting in a large amount of noise, as well as more aerodynamic drag and thus a higher fuel consumption [1]. Morphing technology is capable of providing a solution to these two inconveniences, as a wing which implements it can change its shape without forming those discontinuities.

Much research has already been done into morphing wing and airfoil designs. A way to design an optimum target shape regarding structural weight and aerodynamic performance has been developed by A. de Gaspari and S. Ricci [2]. Other research has been done by B.K.S. Wood and M.I. Friswell [3]. They

have been investigating the use of a fishbone shaped structure to minimize the actuation energy needed. This research resulted in a functional wooden prototype for a morphing trailing edge structure. Regarding the choice of the material, S. Kota et al. [4] have been researching which material is the optimal choice in a morphing structure for the skin. They found that the complete mechanism should consist of one type of material to minimize the weight. In the field of noise and aerodynamic drag, research has been done with respect to drag reduction by H. Suzuki, K. Rinoie, and A. Tezuka [5]. Lastly, the effect of morphing technology on noise reduction has been elaborated by D.P. Lockard and M.M. Choudhari [6].

Most of those papers explain theoretical research and they did not investigate the concept from a structural and experimental perspective. Therefore, this paper has been written to evaluate the morphing leading edge concept from a structural point of view. The current research has been done as a part of the CleanSky Green Regional Aircraft Integrated Technology Demonstrator, which focuses on the LeaTop (Leading Edge Topology) project in particular [7]. The main goal of that project is to provide a functional demonstrator in which leading edge morphing technology has been implemented to prove that such a system would work in reality. In this paper a broad structural analysis of the behaviour of the skin is presented.

Three different types of tests and simulations have been performed by the group responsible for the LeaTop demonstrator [7]: Finite Element Method (FEM) simulation, experimental strain measurements and pictures taken during the deformation of the demonstrator. The resulting data was provided in order to perform the analyzes presented in this paper.

The research aims at evaluating the viability of the LeaTop demonstrator. To achieve this, first, an explanation for the comparison of the experimental strain data and the data generated by the FEM analysis is given. Second, the loading of the structure and the maximum leading edge rotation is investigated in order to determine if it complies with the requirement of a minimum rotation angle of 5°. Third, it is analyzed whether the structure is under pure bending and why this is favourable. Additionally, this paper determines whether the actual deformed shape matches the target shape. Finally it is investigated if the LeaTop is a reliable fail-safe design.

II.   Methods

Three types of data have been analyzed in the context of this research: strain data gathered during the extension of the actuator, strain data from the FEM model and images taken during the extension test. First, the experimental strain data is elaborated on, followed by the FEM strain data and finally the image processing is explained.
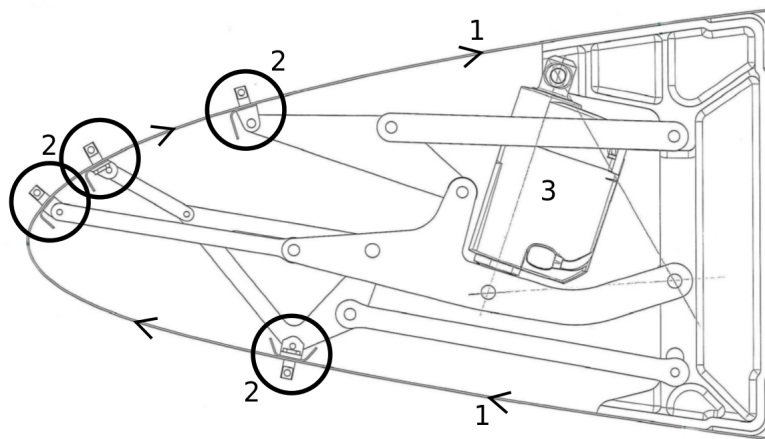
Figure 1. Illustration of the LeaTop demonstrator. The strain measured by the optical fibre is mapped in the shown direction (1). The four stringers (2) are attached to the skin and the actuator (3) is placed in the middle of the structure. Adapted from [7].

A Experimental strain measurement

The mechanism was tested by extending the actuator from the rest position (0 mm extension) up to the maximum extension of 39.2 mm. A cross-section of the demonstrator can be seen in Fig. 1. During the test, the strain was measured at every 1.3 mm along the arcwise direction using one optical fibre. This optical fibre measures the strain in the structure using a method called Fiber Bragg Grating [8]. The optical fiber was fitted to the leading edge on the inner and outer surface at two separate locations, placed on either side of the actuation mechanism. The external contours are labeled A and B, while the internal contours are labeled C and D (see Fig. 2).

Since the strain is measured with one continuous optical fibre that runs through these four contours, the measurements are to be divided in four intervals, relating to the contours A through D. These intervals need to be linearly mapped to the correct arclength, e.g. the contour A measurements are mapped from [1.59, 2.6] in the optical fiber to [1.05, 0.05] in terms of arclength. It should be noted that the origin of the arclength coordinate system lies at the bottom of the demonstrator (see Fig. 1), whereas two contours (A and D) of the fibre start from the top (see Fig. 2). For these contours the direction has to be reversed in order to compare them to the other contours. On the inside, four stiffeners were placed to improve structural rigidity (as seen in Fig. 1), which restricted the optical fibre (contours C and D) . As such, the fibre could not be fitted to the skin at the stringer locations. Since the two middle stringers were close together, the fibre was not attached in-between them. Therefore, there are three unattached fibre segments measuring no strain, and thus provide no information. This is why contours C and D contain four intervals of different lengths that are linearly mapped to the correct fiber length.
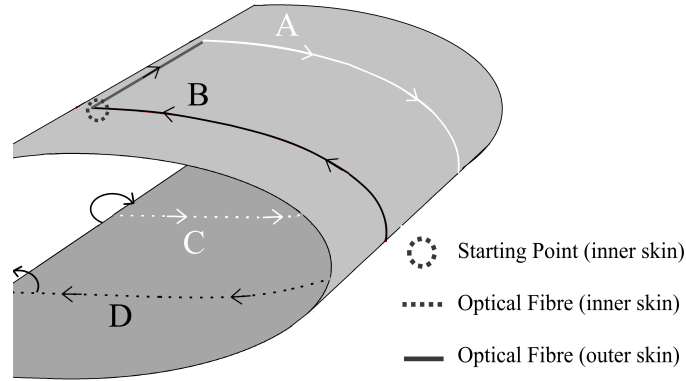

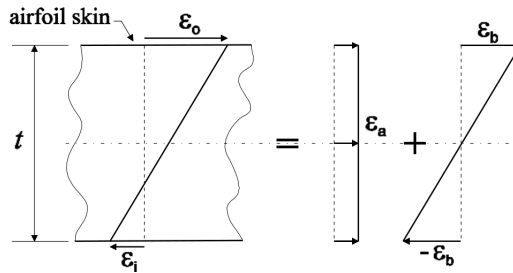**Figure 2. Illustration of the optical fibre contours**

Figure 3. An illustration of a combined axial and bending strain state [7].

By measuring the strain on both sides of the skin, it is possible to determine the axial and bending strain components (see Fig. 3). The maximum value of the latter can be computed as $\varepsilon_b = \pm(\varepsilon_o - \varepsilon_i)/2$. On the other hand, the axial strain is assumed to be constant through the thickness and it can be calculated as the average between the two edge values $(\varepsilon_o, \varepsilon_i)$. For these calculations it is necessary that the strain values at the exact same arcwise location are selected (only on opposite sides). However, the data points do not lie at the same locations. Therefore, it was necessary to interpolate the data from both the inner

and outer contours to match this discrepancy. A linear spline interpolation was chosen, which in general can be described by Eq. (1), where $f(x)$ is the function value at position x and the index i represents the data point before the x-location. Since the points are only spaced 1.33mm apart from each other, a linear spline interpolation gives a good accuracy.

$$f(x) = f(x_i) + \frac{f(x_{i+1}) - f(x_i)}{x_{i+1} - x_i} \cdot (x - x_i) \tag{1}$$

B   FEM strain analysis

To predict the strains in the structure, FEM software was used to obtain the strain data, given in a Cartesian coordinate system. This strain data was provided by the the group responsible for the LeaTop demonstrator [7]. To compare the FEM data with the measurements, the coordinate system had to be rotated using the transformation matrix in Eq. (3), since the optical fibre measures the strains along the arc (see Fig. 1). The transformation matrix Q is a passive counter-clockwise rotational matrix around z-axis (the depth axis). More on passive transformation matrices can be found in 'Lectures on analytic and projective geometry' by Dirk J. Struik [9]. In the following matrix $\tilde{\varepsilon}_{ij}$ is the transformed strain tensor value, ε_{ij} is the given strain data tensor value, and θ is the angle of rotation.

$$\tilde{\varepsilon} = Q \cdot \varepsilon \cdot Q^T \tag{2}$$

$$\begin{bmatrix} \tilde{\varepsilon}_{xx} & \tilde{\varepsilon}_{xy} & \tilde{\varepsilon}_{xz} \\ \tilde{\varepsilon}_{yx} & \tilde{\varepsilon}_{yy} & \tilde{\varepsilon}_{yz} \\ \tilde{\varepsilon}_{zx} & \tilde{\varepsilon}_{zy} & \tilde{\varepsilon}_{zz} \end{bmatrix} = \begin{bmatrix} \cos\theta & \sin\theta & 0 \\ -\sin\theta & \cos\theta & 0 \\ 0 & 0 & 1 \end{bmatrix} \cdot \begin{bmatrix} \varepsilon_{xx} & \varepsilon_{xy} & \varepsilon_{xz} \\ \varepsilon_{yx} & \varepsilon_{yy} & \varepsilon_{yz} \\ \varepsilon_{zx} & \varepsilon_{zy} & \varepsilon_{zz} \end{bmatrix} \cdot \begin{bmatrix} \cos\theta & -\sin\theta & 0 \\ \sin\theta & \cos\theta & 0 \\ 0 & 0 & 1 \end{bmatrix} \tag{3}$$

The FEM data was provided in step increments along the skin such that a finite number of points represent the skin and each point has its tensor, shown in Eq. (2) and (3). In order to get θ, the slope between each two points was calculated. The angle of rotation is taken such that after the transformation, data which was in the x-direction before would become tangent to the skin. Similarly, data previously being in y-direction is rotated so that it would become normal to the skin pointing outward. This was repeated for the slope between each set of consecutive points until all points were covered. This can better be observed in Fig. 4. Note that the skin contour starts at **a** and moves towards **b**.
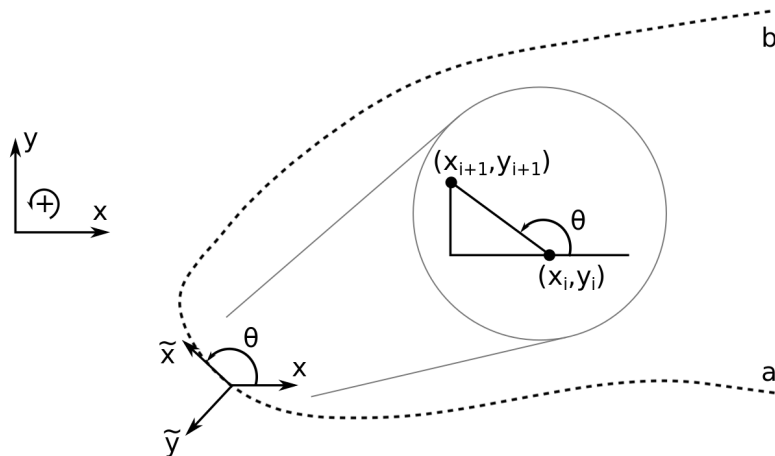

Figure 4. Angle rotation along the contour

C   Image Recognition technique

To compare the physical deformation to the FEM data a digital camera was used to take several photographs of the deformed airfoil at different load steps. To make it easier to algorithmically determine the shape of the leading edge, a bright red wire was used to mark the edge of the structure. An example of one of the images can be seen in Fig. 5a. The various images were processed by an image recognition algorithm written in Python. This process can be seen in Fig. 5b and Fig. 5c. First, the red color was amplified and turned into grayscale images. Then, using the scikit-image package, an edge detection algorithm was used to find the edges of the wire [10]. Finally, the edge data of the wire was averaged to generate a curve representing the curvature of the airfoil. The graphs of different comparisons were plotted using Python. The fully deformed airfoil was then compared to the target shape. In addition, the graph of the FEM data was also compared to the plots using the experimental data.

To determine the angle of rotation of the deformed model relative to the original shape, the position of the rightmost point of each shape was determined relative to the origin. From these two direction vectors, the angle of rotation between the two was calculated.
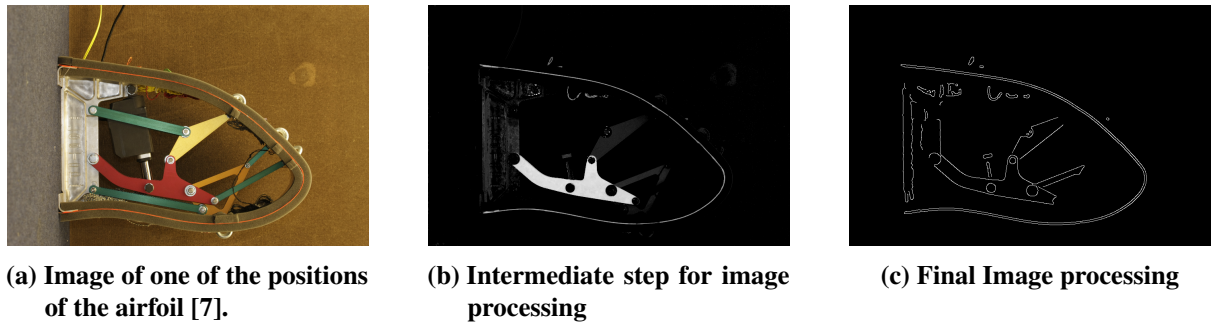

(a) Image of one of the positions of the airfoil [7].

(b) Intermediate step for image processing

(c) Final Image processing

Figure 5. Image Recognition technique

III.   Results and Discussion

After the data analysis was performed, the strains obtained from the FEM and optical fibre were analyzed and compared. Furthermore, the shape deformation of the leading edge was obtained from the image processing, then compared with the intended aerodynamic shape and the FEM prediction.
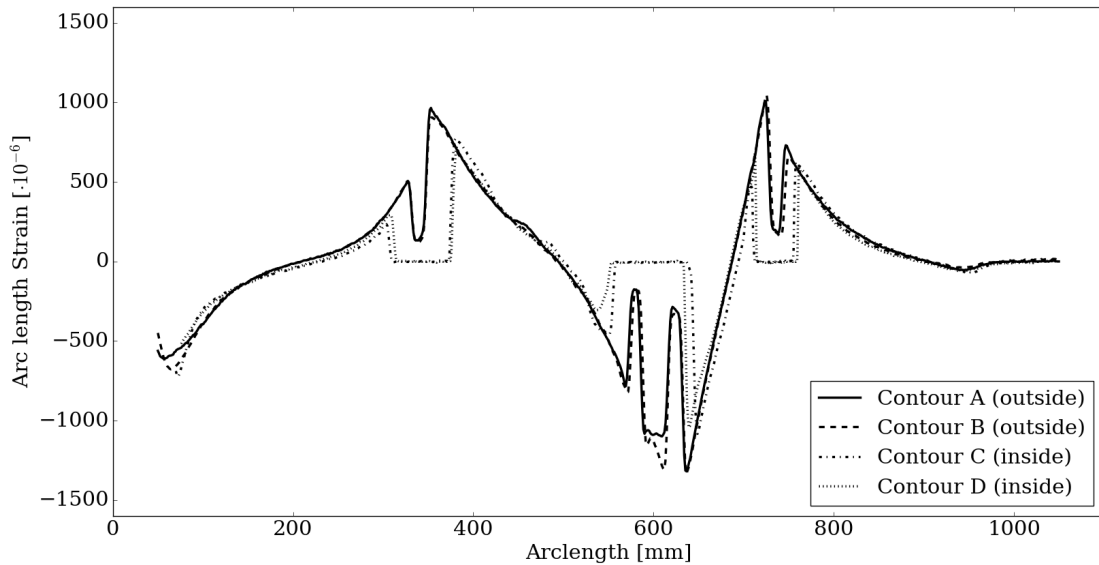

Figure 6. Strain measurements at different contours. Actuator displacement: 10 mm

A   Strain Analysis

The results from the optical fibre tests were compared with the FEM data. Two measurement locations, as illustrated in Fig. 2, were chosen to ensure reproducibility of the experiment and the strains resulting from these two locations (both on the inside and outside of the demonstrator) are compared in Fig. 6. The strain was measured on the outer and inner skin, labeled ε_o and ε_i respectively. In the plots, the inner skin strain values were multiplied by -1 in order to better compare them with the outer skin.
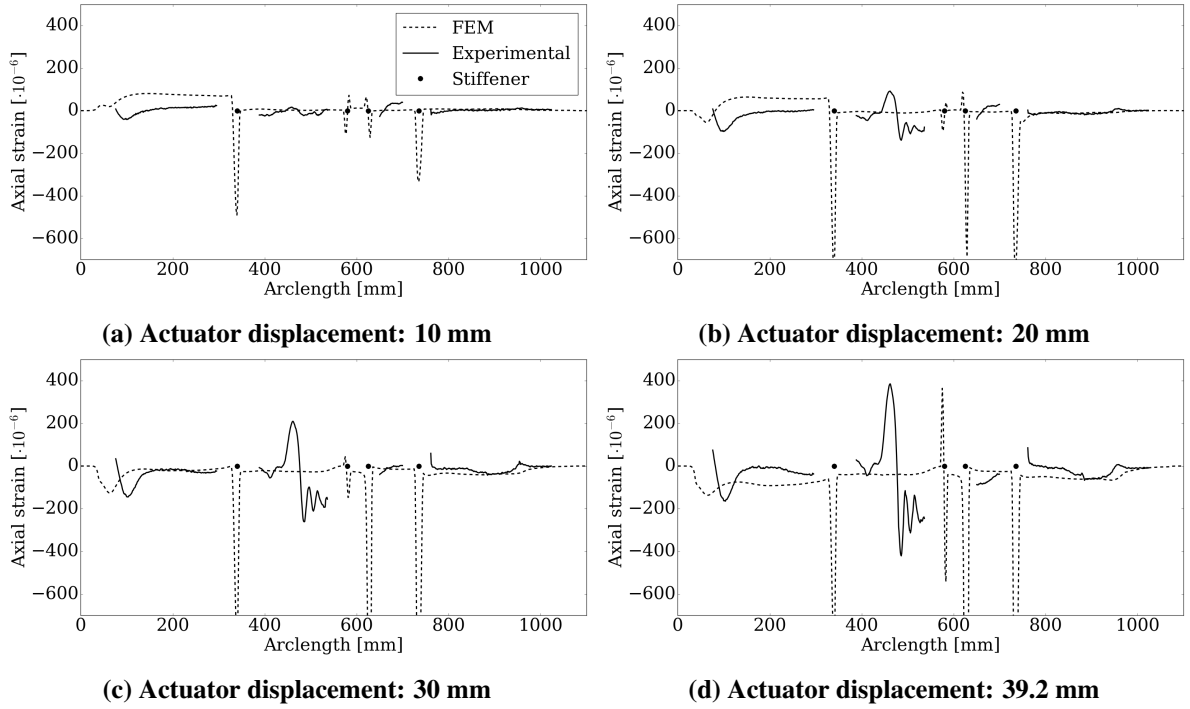
The strain is plotted as a function of arc-length, starting from the bottom of the demonstrator. First, it can be seen that the strain at the two measurement locations overlaps very closely. This indicates that the strain is independent of the spanwise location: the structure does not twist. Second, as it can be seen in Fig. 3, if the skin is under pure bending, the strains are equal in magnitude but opposite in signs. The inner strains match the outer strains (when multiplied with -1) with only little deviation, showing that the deformation is mostly due to bending and not elongation. Third, it should be noted that the inner strains curves have regions where the strain is 0. These are the locations where the optical fibre is not attached to the skin due to the stringers, thus not measuring any strain. Only the strain measurements for an actuator displacement of 10 mm are shown here, the other load steps can be found in Appendix A.

(a) Actuator displacement: 10 mm   (b) Actuator displacement: 20 mm

(c) Actuator displacement: 30 mm   (d) Actuator displacement: 39.2 mm
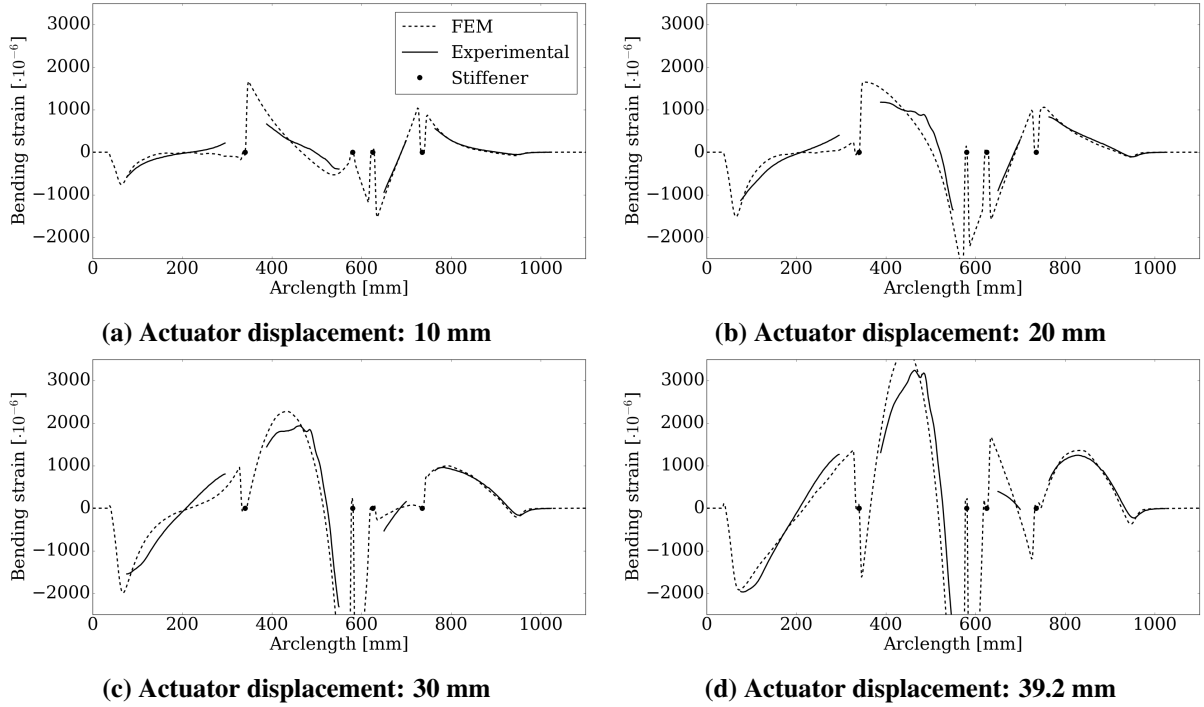
Figure 7. Comparison between the FEM and experimental bending strains at different load steps

The bending strains and axial strains are obtained by decomposing the total inner and outer strain (which can be found in Appendix B) as shown in Fig. 3. The bending strains are plotted for the four load steps in Fig. 7. The experimental graph is piecewise due to the lack of data on the inner skin in the previously mentioned intervals. It can be seen that the experimental strains are similar to the FEM across the entire arc length. The interval 300 mm to 700 mm has the highest strain values, with only minor deviations between the FEM and optical fibre data in this region. One of the reasons for these discrepancies is due to the fact that the stringers in the numerical model are part of the skin, whereas in the experiment, the stringers are separate pieces which are attached using rivets. This means that in the experiments the load transfer between stringer and skin is different compared to the FEM, highlighting the model errors of the latter.

Nevertheless, the strain at the stringer positions is zero for the FEM analysis, as expected since the stiffeners are completely rigid in the FEM model. The experimental data does not exactly go to 0 because it is not possible to have a perfectly rigid stringer in an experiment as in the FEM.

(a) Actuator displacement: 10 mm

(b) Actuator displacement: 20 mm

(c) Actuator displacement: 30 mm

**(d) Actuator displacement: 39.2 mm**

Figure 8. Comparison between the FEM and experimental axial strains at different load steps

The axial strain comparison between the FEM and optical fibre is shown in Fig. 8. The FEM strains shows peaks around the stringer locations, which is unexpected since the stringers are considered rigid. Although the bending strains are an order of magnitude higher than the axial strains, the latter should not be neglected around the stringers due to the large excitations that the FEM data predicts. Farther away from the stringers the behaviour is dominated by the bending strain.

Since the shear strains were provided by the FEM analysis, after the transformation, it was decided to observe the shear strains in the new coordinate system. The plot of τ_{xy} vs arc-length and τ_{xz} vs arc-length are shown in Fig. 9. It can be seen that the order of magnitude of the shear strain is negligible compared with the bending strains. From this it can be concluded that the shear strain can be neglected and that the skin is under pure bending. However, no comparison can be made with the experiment, as there is no experimental measurement on the above mentioned shear strains.

Principle strains are a combination of axial strains, bending strains and shear strains. However, as stated earlier, the skin is almost under pure bending, since the axial and shear strains can be neglected, except at the stringers, where large axial strain values are predicted. This is desirable since the bending strains are easy to measure, which makes failure prediction easier. Bending strains are favourable above axial strains, since bending strains induce no compressive forces and therefore avoid buckling of the skin.

(a) Shear strain in the xy direction

(b) Shear strain in the xz direction
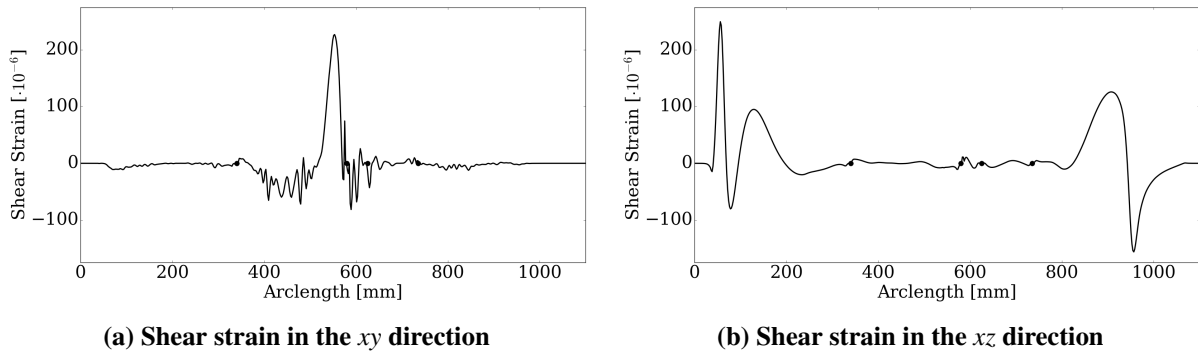
Figure 9. The shear strain at 39.2 mm deflection

B   Image Recognition Technique

In the experiment, the actuator length was increased from 0 mm to 39.2 mm in steps of 2.5 mm. The incremental change in shape can be observed in Fig. 10a. The contour lines show the airfoil shape in relation with the extension by the actuator. Moreover, as it was important to have a comparison of the experimental results with the FEM results, Fig. 10b shows the comparison for four actuator displacements. When the actuator extends to 39.2 mm, the demonstrator should match the target shape. From the figure it can be noted that the morphed wing matches the airfoil shape properly except for a few points.

<div style="display:flex;justify-content:space-between;">
<div>

(a) Experimental Results

</div>
<div>

(b) Experimental Results compared to FEM

</div>
</div>
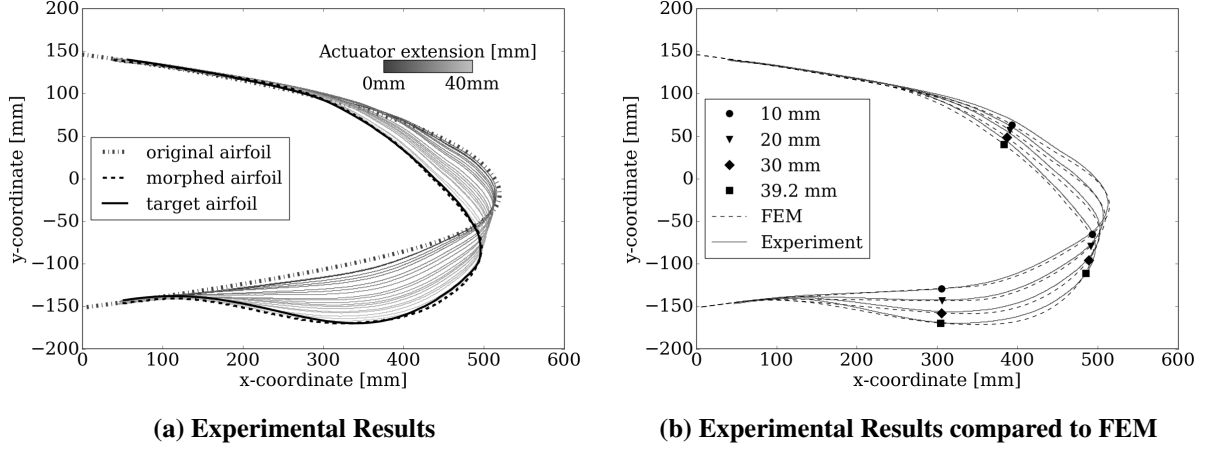
Figure 10. Geometrical comparison of the morphed leading edge

The difference in target shape and the experimental results can mostly be seen in the bottom part of the airfoil. During the experiment it was observed that the lower skin separated from the spar due to the failure of the adhesive. In addition, the actuator used in the experiment was larger than originally intended in the design. This caused an extension of 7mm instead of 0mm in its fully contracted state, which meant that the airfoil was already deformed. This resulted in a deviation from the target shape.

While writing the image recognition algorithm a difficulty was encountered when analysing the images, as the camera was not kept stationary during the experiment. This resulted in small random translations in the graphs, causing the airfoil to be shifted slightly. This did not noticeably distort the data, but did decrease the accuracy. In future experiments, the camera should be held with more stability by fixing the position of the tripod then placing the camera on it.
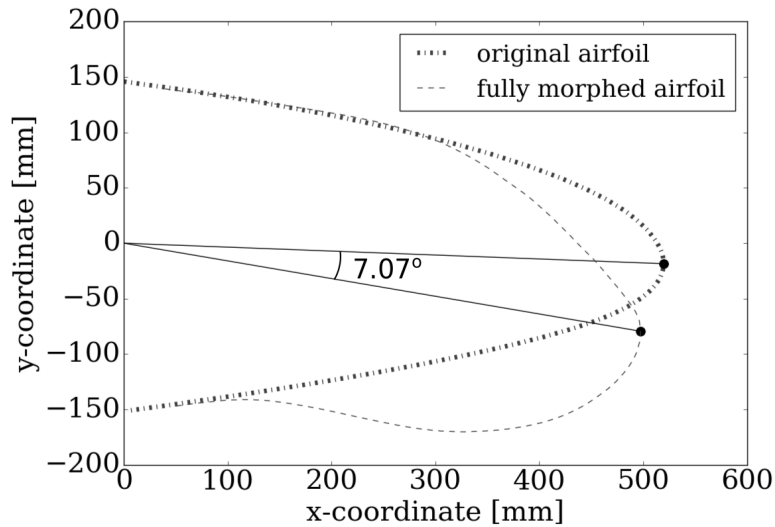
Figure 11. Rotation analysis

Figure 11 shows a total rotation of 7.07° of the leading edge, which is in agreement with the requirement of a rotation of 5°. The difference of 2.07° can be interpreted not as an error, but as an over-design of the demonstrator. The developed algorithm takes the tip of the airfoil as a reference value. Furthermore, the accuracy of the rotation angle is influenced by the image processing algorithm and the choice of the reference point. Using the same method, the deflection of the target shape was determined to be 8.13°. A difference of 1.05° of deflection is found at the maximum deflection of the leading edge.

C   Discussion on Reliability of the LeaTop Mechanism

From the comparison of the predicted FEM strain data to the optical fibre strain measurements, it can be concluded that even through the FEM and optical fibre measurements overlap very closely, they do not exactly match. These deviations are mainly caused by the assumption that the stringers are rigid. Furthermore, the adhesive on the bottom skin was not able to keep the structure completely intact at higher loads.

It is hard to determine for certain whether LeaTop is a fail-safe design without more detailed analysis specifically on reliability. There are, however, several remarks that could be considered at this point. The morphing leading edge is a very complicated mechanism with a lot of moving parts. In general, the more parts- the more likely one of them could fail. Though the failure of some of these parts may not be as catastrophic as others, the deformation of the skin will definitely be different than required if one of them breaks. This means that in case of a take-off and landing (where the leading edge will be morphed), the deformation could make the wing not generate the required lift. Furthermore, having one wing shape different than the other will most likely create a difference between the lift generated by both wings. This could induce an unexpected roll force on the aircraft, which is undesirable when the aircraft is close to the ground. Even though there is the same possibility with conventional slats and slots, because they have a lot less moving parts, they are less likely to experience a failure.

IV.   Conclusion

This paper aims to analyze the performance of the LeaTop demonstrator, meaning the effectiveness of the mechanism, the structural behaviour and its ability to match the target shape. After the experiment was done by the group responsible for the LeaTop demonstrator, the results acquired show that the design requirements to show at least 5° leading edge rotation and to match the prescribed target shape as close as possible have been met successfully.

The comparison between the axial and bending strains showed that the bending strains dominate. However, it cannot be considered to be under pure bending around the stringers, because there are still peaks of axial strains. The xy-strains can be neglected and thus, concluded that the regions of the skin with no stringers are predominantly under bending. This is desirable since the bending strains do not cause compressive forces and therefore prevent buckling.

By considering the airfoil shape measurement, it can be concluded that the target airfoil matched the morphed shape except for a few points, most notably around the bottom part of the airfoil, where the glued joint failed. Additionally, due to the actuator being larger than the original design intended, the mechanism was already deformed in the actuators most contracted state. Furthermore, it was found that the maximum achieved tip rotation appears to be 7.07 degrees. This might have been affected due to the movement of the camera, influencing the output of the algorithm.

The LeaTop mechanism is not fail-safe. This is due to a combination of its complexity and the crucial conditions it is used during take-off and landing. So at this point it is impossible to predict what the shape of the leading edge would be in case of a failure. One of the next steps in the future would be to analyze the mechanism deformation when different parts fail.

Several improvements can be made to further experiments. The camera should be fixed in one location, so as to minimize the random shifting between pictures. Furthermore, some reference points could be added to the leading edge and its attachment, to display their relative movement better and provide additional calibration accuracy. Finally, improvements could be made to the structure regarding

the bond between the frame and the skin. The glue joint which failed should be replaced by a stronger joint. This could be done by, for example, using a stronger glue, perhaps in combination with a riveted or welded joint. The next step regarding the structural analysis of morphing leading edges would be a fatigue research.

References

[1] ACARE, *2008 Addendum to the Strategic Research Agenda*, URL: `http://www.acare4europe.org/`, [cited: 10 March 2016].

[2] De Gaspari, A. and Ricci, S., "A two-level approach for the optimal design of morphing wings based on compliant structures", *Journal of Intelligent Material Systems and Structures*, Vol. 22, No. 10, 2011, pp. 1091–1111.

[3] Woods, B. K. S. and Friswell, M. I., "Preliminary investigation of a fishbone active camber concept", *ASME 2012 Conference on Smart Materials, Adaptive Structures and Intelligent Systems*, American Society of Mechanical Engineers, 2012, pp. 555–563.

[4] Kota, S. et al., "Design and application of compliant mechanisms for morphing aircraft structures", *Smart Structures and Materials*, 2003, pp. 24–33.

[5] Suzuki, H., Rinoie, K., and Tezuka, A., "Laminar airfoil modification attaining optimum drag reduction by use of airfoil morphing", *Journal of Aircraft*, Vol. 47, No. 4, 2010, pp. 1126–1132.

[6] Lockard, D. P. and Choudhari, M. M., "Noise radiation from a leading-edge slat", *AIAA paper*, Vol. 2009-3101, 2009.

[7] Sodja, J. et al., "Experimental Evaluation of the Morphing Leading Edge Concept", *23rd AIAA/AHS Adaptive Structures Conference*, 2015, p. 791.

[8] Güemes, A., Fernández-López, A., and Soller, B., "Optical fiber distributed sensing-physical principles and applications", *Structural Health Monitoring*, 2010.

[9] Struik, D. J., "Lectures on analytic and projective geometry", Courier Corporation: New York, 2011, chap. 4.

[10] Van der Walt, S. et al., *scikit-image: image processing in Python*, version 0.11.3, June 2014, DOI: `10.7717/peerj.453`, URL: `http://dx.doi.org/10.7717/peerj.453`.
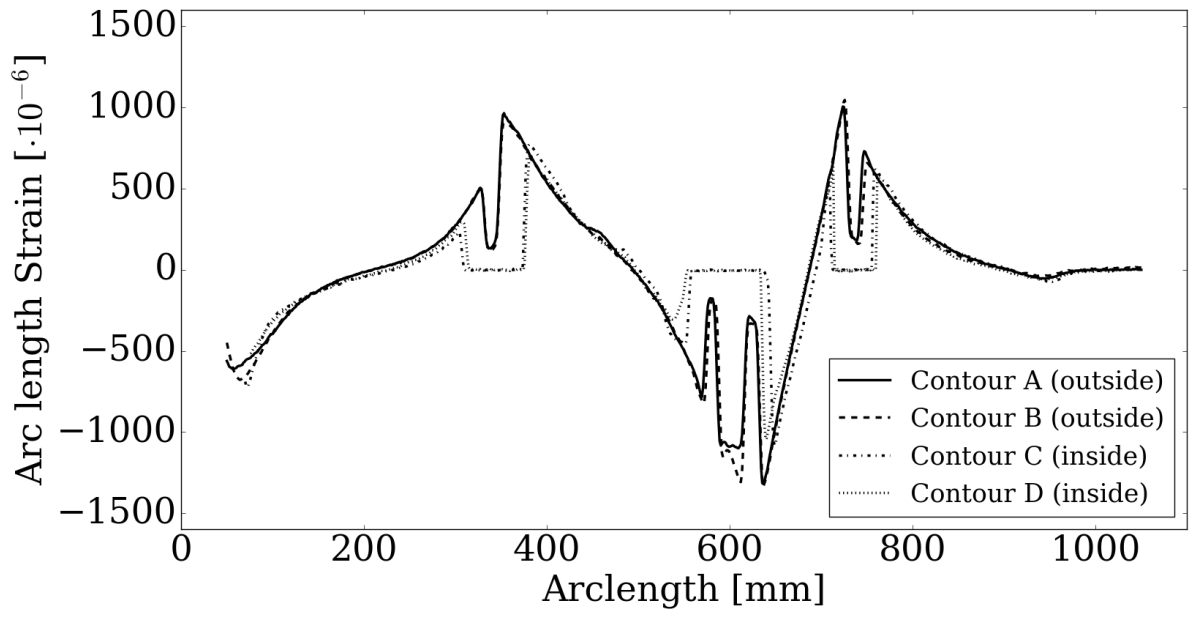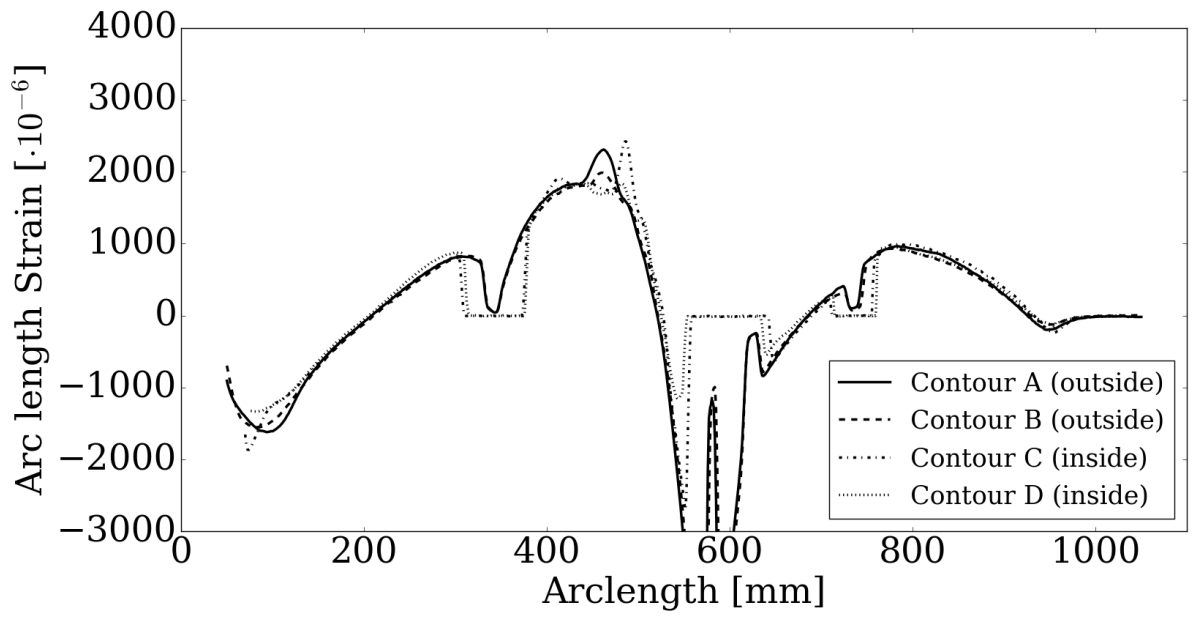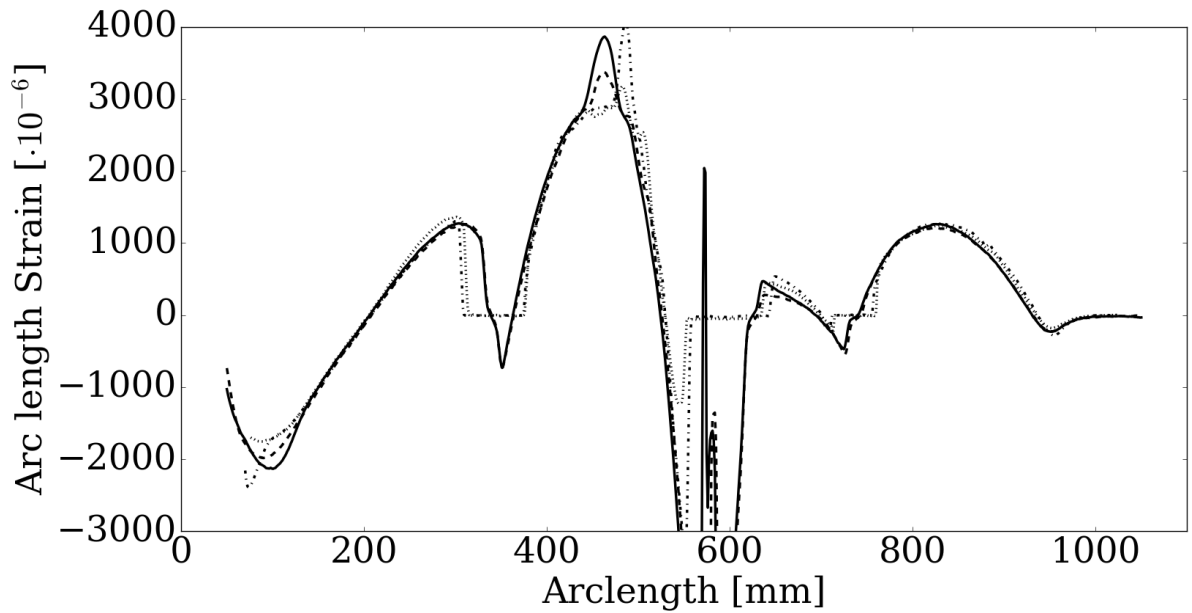
(a) Actuator displacement: 10mm
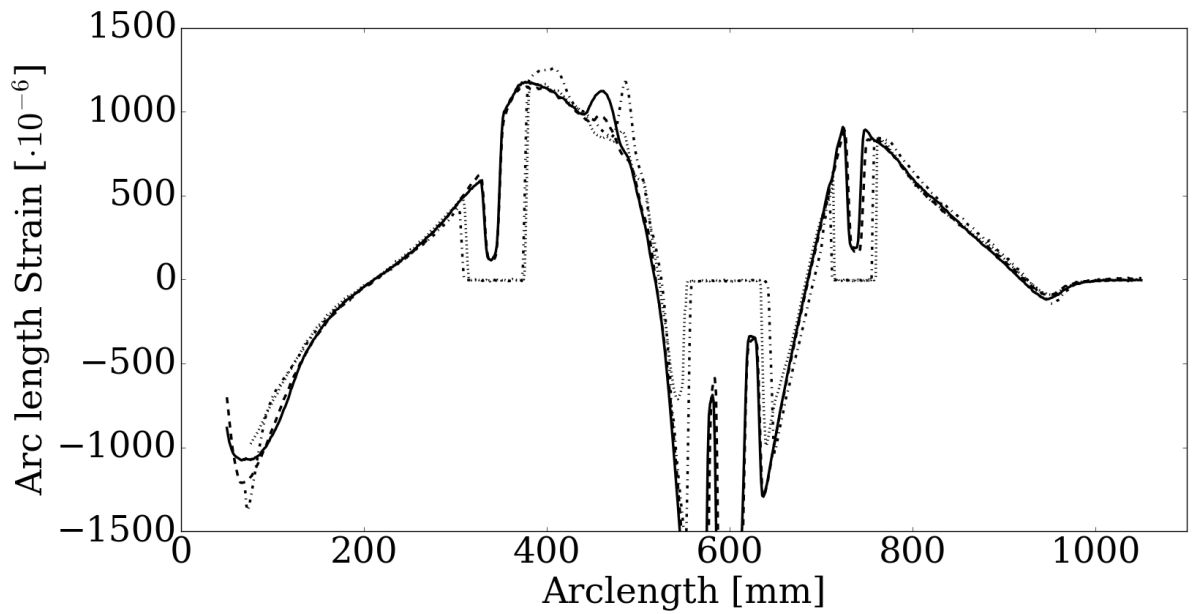
(b) Actuator displacement: 20mm

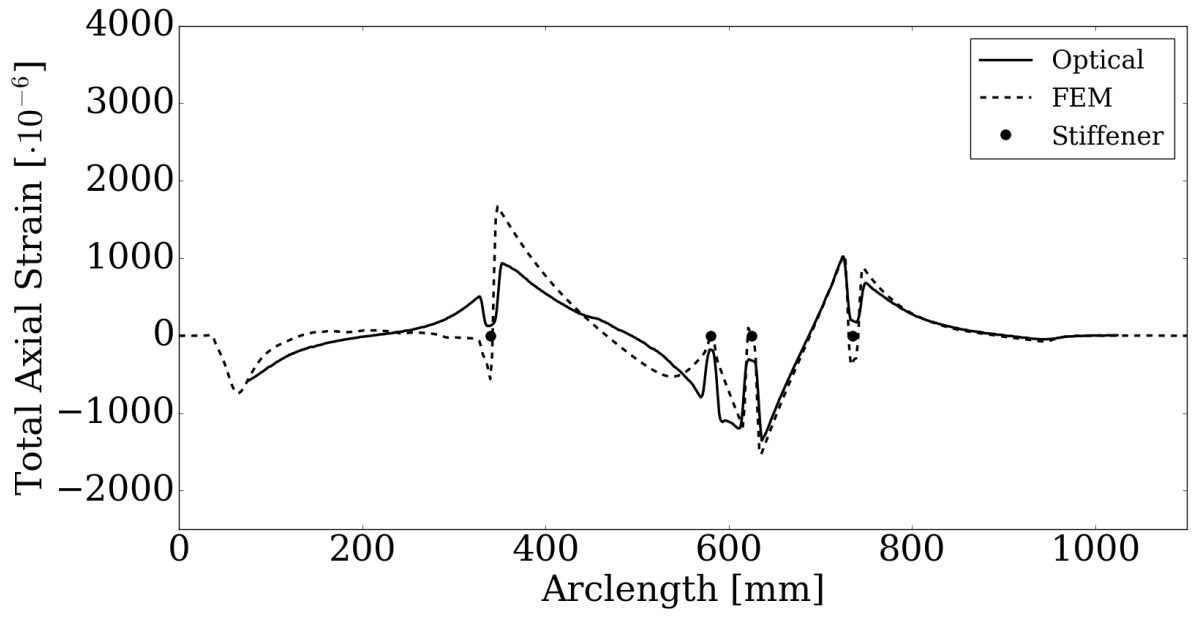**Figure 12. Comparison between the strain measurements at contours A, B, C and D**
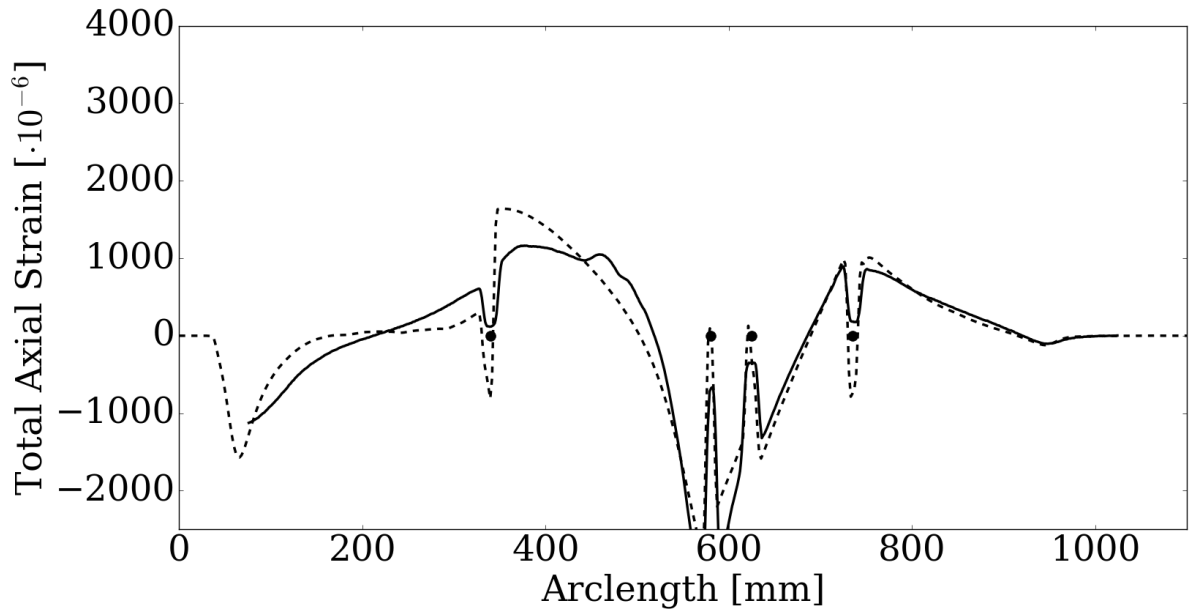
(a) Actuator displacement: 30mm

(b) Actuator displacement: 39.2mm

Figure 13. Comparison between the strain measurements at contours A, B, C and D
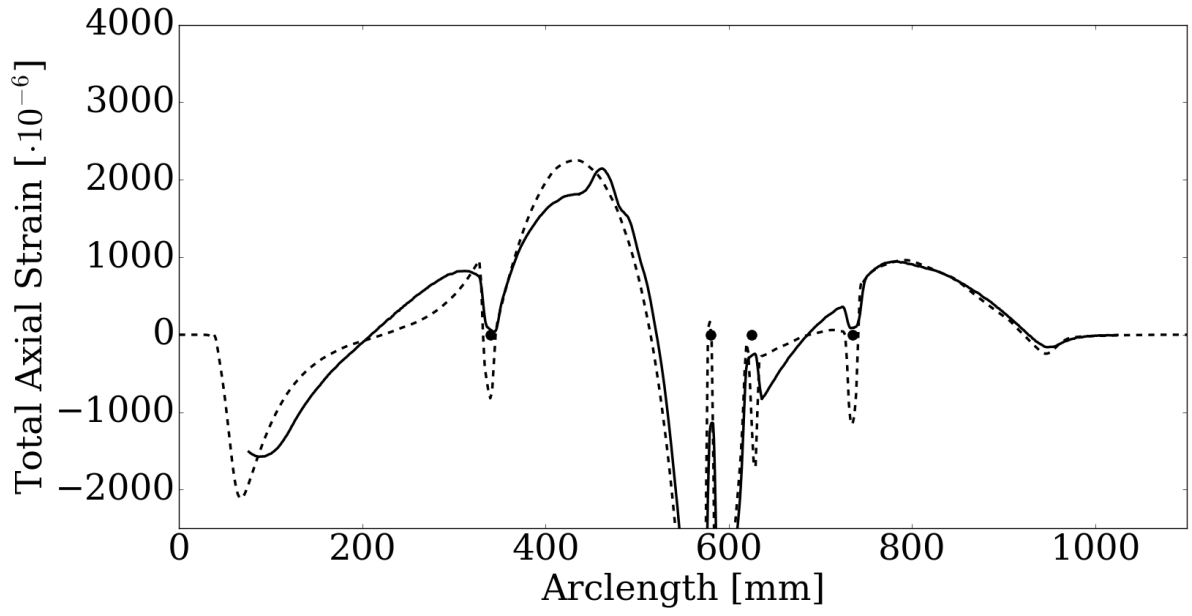
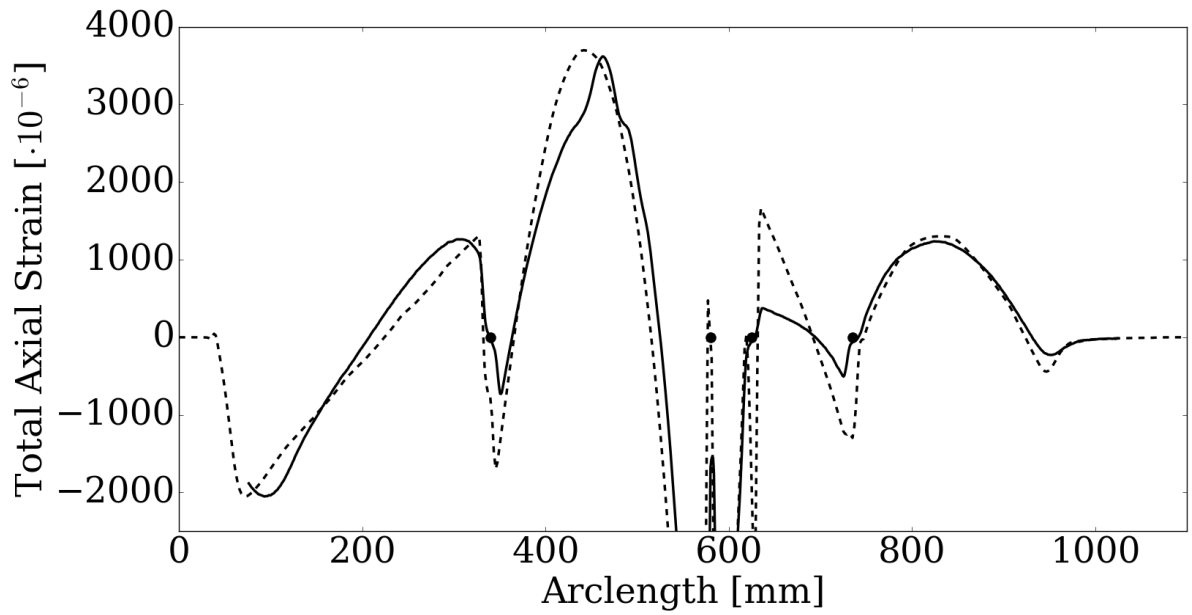**(a) Actuator displacement: 10mm**

(b) Actuator displacement: 20mm

Figure 14. Comparison between the total strain measurements and the FEM on the outer skin

(a) Actuator displacement: 30mm

(b) Actuator displacement: 39.2mm

Figure 15. Comparison between the total strain measurements and the FEM on the outer skin